AGU100 ADVANCING EARTH AND SPACE SCIENCE

Paleoceanography and Paleoclimatology

RESEARCH ARTICLE

Key Points:
- Carbonate ion increased at the intermediate-depth SW Atlantic during HS1, coeval with initial atmospheric CO_2 rise
- Carbonate ion signal is most likely due to reduction in remineralized carbon, pointing to a biological pump driver
- Tracer inversion results suggest intermediate-depth sites in subtropical South Atlantic can be used to infer SAZ productivity

Supporting Information:
- Supporting Information SI

Correspondence to:
M. Lacerra,
mlacerra@princeton.edu

Less Remineralized Carbon in the Intermediate-Depth South Atlantic During Heinrich Stadial 1

Matthew Lacerra[1,2] (iD), David C. Lund[1] (iD), Geoffrey Gebbie[3] (iD), Delia W. Oppo[4] (iD), Jimin Yu[6] (iD), Andreas Schmittner[7] (iD), and Natalie E. Umling[4,5] (iD)

[1]Department of Marine Sciences, University of Connecticut, Groton, CT, USA, [2]Now at Department of Geosciences, Princeton University, Princeton, NJ, USA, [3]Department of Physical Oceanography, Woods Hole Oceanographic Institution, Woods Hole, MA, USA, [4]Department of Geology and Geophysics, Woods Hole Oceanographic Institution, Woods Hole, MA, USA, [5]Department of Earth and Planetary Sciences, American Museum of Natural History, New York, NY, USA, [6]Research School of Earth Sciences, Australian National University, Acton, ACT, Australia, [7]College of Earth, Ocean, and Atmospheric Sciences, Oregon State University, Corvallis, OR, USA

Abstract The last deglaciation (~20–10 kyr BP) was characterized by a major shift in Earth's climate state, when the global mean surface temperature rose ~4 °C and the concentration of atmospheric CO_2 increased ~80 ppmv. Model simulations suggest that the initial 30 ppmv rise in atmospheric CO_2 may have been driven by reduced efficiency of the biological pump or enhanced upwelling of carbon-rich waters from the abyssal ocean. Here we evaluate these hypotheses using benthic foraminiferal B/Ca (a proxy for deep water $[CO_3^{2-}]$) from a core collected at 1,100-m water depth in the Southwest Atlantic. Our results imply that $[CO_3^{2-}]$ increased by 22 ± 2 μmol/kg early in Heinrich Stadial 1, or a decrease in ΣCO_2 of approximately 40 μmol/kg, assuming there were no significant changes in alkalinity. Our data imply that remineralized phosphate declined by approximately 0.3 μmol/kg during Heinrich Stadial 1, equivalent to 40% of the modern remineralized signal at this location. Because tracer inversion results indicate remineralized phosphate at the core site reflects the integrated effect of export production in the sub-Antarctic, our results imply that biological productivity in the Atlantic sector of the Southern Ocean was reduced early in the deglaciation, contributing to the initial rise in atmospheric CO_2.

1. Introduction

One of the defining features of the last deglaciation is the 30-ppmv rise in atmospheric CO_2 early in Heinrich Stadial 1 (HS1; 17.5–14.5 kyr BP; Monnin et al., 2001; Lourantou et al., 2010). Changes in mean global temperatures lagged atmospheric CO_2 by ~500 years throughout the deglaciation (Shakun et al., 2012), suggesting that atmospheric CO_2 was a primary driver of Earth's transition from a glacial to interglacial state. While recent ice core analyses have provided an unprecedented level of detail for the evolution of CO_2 (Marcott et al., 2014), the mechanisms responsible for these changes remain poorly understood. Carbon isotopic analyses of atmospheric CO_2 suggest numerous oceanic and terrestrial processes were viable contributors, making signal deconvolution a difficult task (Bauska et al., 2016). However, new atmospheric $\delta^{13}C$ records from Marine Isotope Stage 3 (which exhibits millennial-scale variability similar to the last deglaciation) imply that atmospheric CO_2 increase during HS1, when the $\delta^{13}C$ of atmospheric CO_2 decreased by 0.3–0.4‰, may be linked to changes in the ocean's biological pump (Bauska et al., 2016; Bauska et al., 2018).

The biological pump is the process by which carbon is exported from the surface ocean as organic material and subsequently remineralized to dissolved inorganic carbon ($\Sigma CO_{2, Rem}$) at depth (Schmittner & Galbraith, 2008). The biological pump affects atmospheric CO_2 through two processes: the soft tissue pump and secondarily through the hard tissue or carbonate pump. The first process acts to draw down atmospheric CO_2 by removing CO_2 (aq) from the surface ocean, decreasing surface water pCO_2, and moving the remaining surface ΣCO_2 pool toward $[CO_3^{2-}]$ (Ito & Follows, 2005). The carbonate pump has the opposite effect, partially counteracting the soft tissue pump by removing alkalinity (ALK) and ΣCO_2 from the surface ocean in a 2:1 ratio and thereby increasing pCO_2 (Hain et al., 2010). In the modern ocean, the soft tissue pump maintains approximately 60–70% of the surface to deep ΣCO_2 gradient. The other 30–40% is maintained by the "solubility pump," a function of overturning circulation strength and physical properties such as temperature and the rate of air-sea gas exchange in regions where surface waters sink into the ocean interior

(Schmittner et al., 2007; Toggweiler et al., 2003). Thus, processes that influence the biological pump may impose a substantial control over atmospheric CO_2 concentrations.

Areas of deep water formation in the North Atlantic and Southern Ocean have disparate levels of biological pump efficiency. High nutrient utilization in waters supplied to the North Atlantic results in North Atlantic Deep Water (NADW) having low preformed phosphate, allowing carbon sequestration in the ocean interior. Less nutrient utilization in the Southern Ocean results in southern sourced Antarctic Bottom Water (AABW) having high preformed phosphate, promoting "leakage" of carbon to the atmosphere (Ito & Follows, 2005). Therefore, global ocean biological pump efficiency may be altered either by a change in the relative proportions of NADW and AABW in the ocean interior or by altering the degree of nutrient utilization in end-member surface waters. Note that while we use the term *biological pump efficiency* to describe the completeness of nutrient consumption in surface waters (e.g., 0–100%), we will also make use of the term *biological pump strength*, a measure of total export production out of the surface mixed layer (e.g., grams per area per unit time).

Here we propose that the initial 30-ppmv rise in atmospheric CO_2 during HS1was driven by reduced global biological pump efficiency, linked to the following: (1) weakening of the Atlantic Meridional Overturning Circulation (AMOC), (2) reduced iron fertilization in the sub-Antarctic Zone (SAZ) of the Southern Ocean, or (3) some combination of these effects. Under a reduced AMOC state, the more efficient northern sourced limb of the overturning circulation (NADW production) ventilates a smaller proportion of the ocean interior, lowering global average biological pump efficiency and raising atmospheric CO_2 (Ito & Follows, 2005). Similarly, reduced efficiency in the Southern Ocean would allow CO_2 to accumulate in the surface ocean, thereby yielding higher atmospheric CO_2 levels.

Model results suggest that AMOC collapse reduces not only biological pump efficiency but also global average biological pump strength (Chikamoto et al., 2008; Schmittner, 2005). Simulations of AMOC collapse using modern boundary conditions result in suppressed upwelling and a reduction in nutrient supply to the global surface ocean, which in turn reduces photosynthesis and export of carbon into the ocean interior (Schmittner, 2005). Reduced export of isotopically light carbon from the surface ocean to intermediate depths (900–1,300 m) decreases the surface-intermediate $\delta^{13}C$ gradient by 0.7–0.9‰ (Schmittner & Lund, 2015). Intermediate-depth records from the Southern Hemisphere show that the benthic foraminiferal $\delta^{13}C$ increase of ~0.3–0.5‰ during HS1 was accompanied by a decrease in planktonic foraminiferal $\delta^{13}C$ of similar magnitude, consistent with the simulated reduction in vertical $\delta^{13}C$ gradient (Bostock et al., 2004; Curry & Oppo, 2005; Hertzberg et al., 2016; Koutavas & Lynch-Stieglitz, 2003; Mix et al., 1991; Pahnke & Zahn, 2005).

Several lines of evidence suggest that the AMOC was weaker during HS1 (e.g., McManus et al., 2004; Chen et al., 2015), making an AMOC reduction a viable mechanism for decreasing biological pump efficiency during HS1. While an AMOC reduction yields substantial changes under modern interglacial conditions, deep waters originating from the surface Southern Ocean during the Last Glacial Maximum (LGM) likely had lower preformed nutrients (Sigman et al., 2010), which combined with an expanded volume of AABW (e.g., Curry & Oppo, 2005) would counteract the effect from a reduction in northern sourced waters. Thus, the maximum influence on atmospheric CO_2 concentrations during HS1 would occur through the combined effect of AMOC collapse and reduced biological pump efficiency in Southern Ocean surface waters.

A likely driver of Southern Ocean biological pump efficiency is wind-driven iron fertilization of the SAZ. In the modern SAZ, phytoplankton are unable to utilize all of the available phosphate and nitrate because their growth is iron limited, making the SAZ a high-nutrient and low-chlorophyll region (Martin, 1990). However, during glacial periods, evidence for greater iron flux within the SAZ, coupled with elevated $\delta^{15}N$ of organic matter bound within the frustules of planktic foraminifera, suggests iron fertilization of the SAZ led to greater utilization of macronutrients and may account for as much as 40 ppmv of the glacial-interglacial atmospheric CO_2 drawdown (Martínez-Garcia et al., 2009; Martínez-García et al., 2014). When wind-blown delivery of iron to the SAZ was curtailed during glacial terminations, nutrient utilization efficiency and export production likely decreased (Martínez-García et al., 2014).

Additional mechanisms may account for the transfer of isotopically light carbon to the atmosphere during the LGM-HS1 transition. Toggweiler et al. (2006) suggested that a poleward shift in westerly winds and

alignment with the Antarctic Circumpolar Current would promote greater divergence in the surface Southern Ocean, resulting in enhanced upwelling of deep waters and outgassing of carbon to the atmosphere. Models that resolve mesoscale eddies in the Southern Ocean show a much weaker overturning response to enhanced westerlies, however (Farneti & Delworth, 2010). Spero and Lea (2002) also proposed that enhanced deep mixing in the Southern Ocean would result in the upwelling of isotopically light, carbon-rich deep waters to the surface, with subsequent transport of the signal to lower latitudes via intermediate and mode waters. While widespread positive $\delta^{13}C$ anomalies observed at intermediate depths during HS1 are inconsistent with this mechanism (Hertzberg et al., 2016), more recent modeling work by Menviel et al. (2018) suggests that liberation of light carbon from the ocean interior during the last deglaciation may cause positive $\delta^{13}C$ anomalies throughout the South Atlantic and South Pacific below 500-m water depth. Considering that both the biological pump and deep liberation mechanisms could account for the observed upper ocean $\delta^{13}C$ anomalies, additional constraints on the carbonate system are required to assess each hypothesis.

In this study, we use benthic foraminiferal B/Ca to evaluate carbon cycling in the intermediate-depth South Atlantic during HS1. Core top calibrations show a positive correlation between benthic B/Ca and the $\Delta[CO_3^{2-}]$ of ambient deep waters (Rae et al., 2011; Yu & Elderfield, 2007). Using the relationship $[CO_3^{2-}] = \Delta[CO_3^{2-}] + [CO_3^{2-}]_{sat}$, and subsequently, $\Sigma CO_2 \approx ALK - [CO_3^{2-}]/0.6$ (Yu et al., 2016), the B/Ca proxy may be used to reconstruct past changes in water-column ΣCO_2 concentrations (Lacerra et al., 2017; Yu et al., 2010; Yu et al., 2016). If enhanced upwelling of carbon-rich water occurred during HS1, then these sites should reflect evidence of higher ΣCO_2 concentrations (Menviel et al., 2018; Spero & Lea, 2002). Such a signal would result in decreasing B/Ca across the LGM-HS1 transition, similar to mid-depth (~2,000 m) Atlantic records that reflect the accumulation of respired carbon associated with collapse of the AMOC (Lacerra et al., 2017; Yu et al., 2010). On the other hand, a weaker biological pump would decrease the export of organic material to depth, lowering the ΣCO_2 content of mode and intermediate waters where the effect of remineralization is greatest (Martin et al., 1987).

In order to reconstruct ΣCO_2 variability during the deglaciation, we analyzed benthic foraminifera from an intermediate-depth Brazil Margin core (KNR159-5-90GGC; 1,105-m water depth). The core site is located within the core of AAIW today (Figure 1) and is complemented by detailed time series of benthic $\delta^{18}O$ and $\delta^{13}C$ (Curry & Oppo, 2005; Umling et al., 2019). We compare our results to the output of a coupled ocean circulation-biogeochemistry model capable of resolving tracer field ($\delta^{13}C$, $[CO_3^{2-}]$, and ALK) responses to variable AMOC (Schmittner et al., 2013). Foraminiferal records show general agreement with model results (Hertzberg et al., 2016; Lacerra et al., 2017; Schmittner & Lund, 2015). Here, for the first time, we evaluate $[CO_3^{2-}]$ results from an intermediate-depth South Atlantic site and assess whether the signal is consistent with model simulations.

Considering core 90GGC is located along the boundary of the South Atlantic subtropical gyre, one would expect this core site to be nonideal for recording past variability in the biological pump. Modeled carbon export at 100-m water depth is low in subtropical gyre settings, suggesting minimal sensitivity to past changes in surface nutrient supply (Siegel et al., 2014). Nonetheless, close to 40% of the PO_4^{3-} in the modern intermediate-depth South Atlantic can be attributed to remineralization (Gebbie, 2014; Ito & Follows, 2005). This discrepancy arises because the remineralization signal at the core site reflects the integrated effect of high-productivity sub-Antarctic surface waters as AAIW flows northward to the Brazil Margin. Thus, a reduction in export production in the sub-Antarctic would be expected to produce a positive B/Ca signal at our core site.

2. Methods

2.1. Core Sampling

Sediment samples were taken from intermediate-depth core KNR-159-5-90GGC (1,105 m; 27.35°S, 46.63°W). Samples were extracted at 2-cm intervals from 30 to 230 cm ($n = 100$), and an additional 15 samples were taken at intermittent levels from the core top to 30 cm. The sediment was freeze-dried, washed through a 63-μm sieve and dried at 40 °C overnight. The existing age model for the core indicates that sedimentation rates (8 to 31 cm/kyr) are sufficient to capture millennial-scale phenomena from the LGM to the
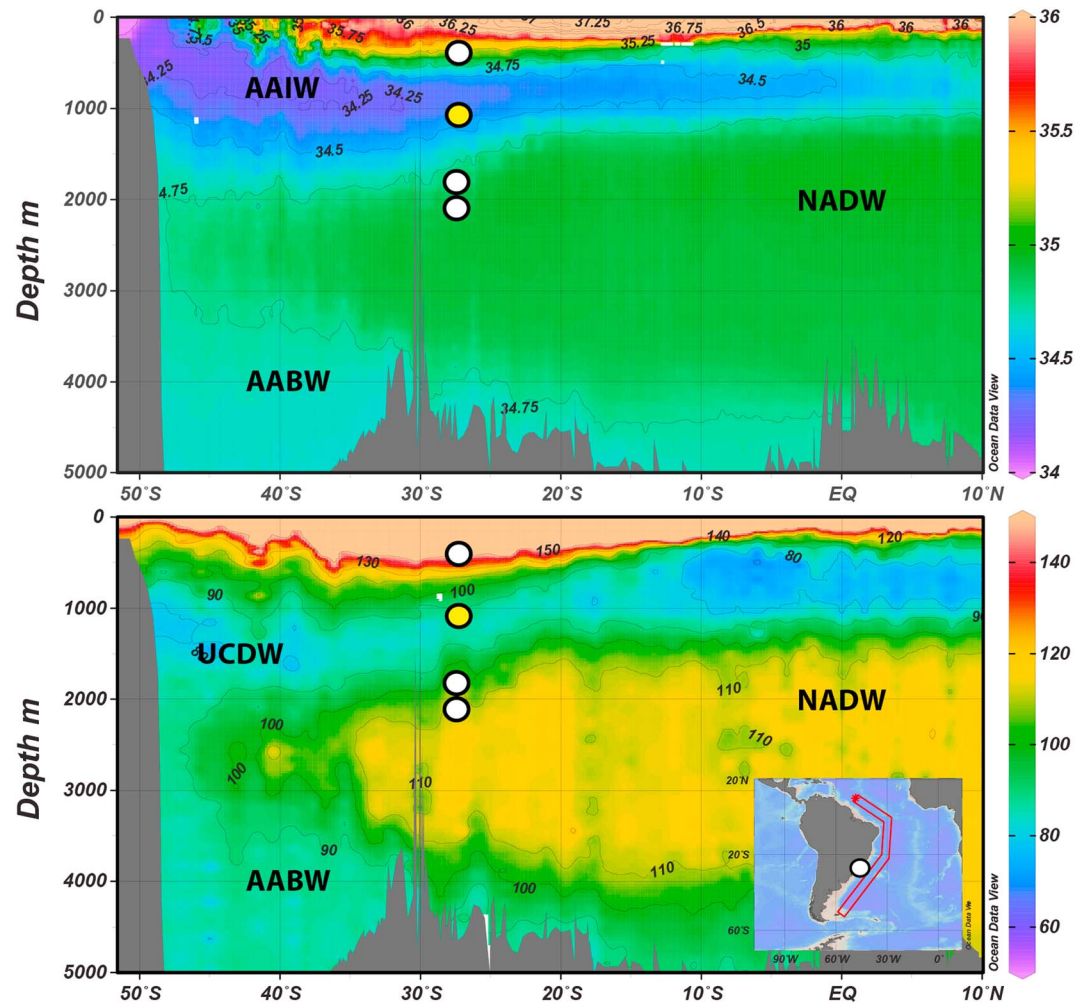
Figure 1. Locations of KNR159-5-90GGC (yellow circle) and supporting Brazil Margin cores (white circles) overlain on a cross section of (top) salinity and (bottom) carbonate ion concentration in µmol/kg from World Ocean Circulation Experiment A17 (Schlitzer, 2015). Contour intervals are 0.25 practical salinity scale and 10 µmol/kg, respectively. The core sites are uniquely positioned to capture different water mass properties in the Southwest Atlantic, including Sub-Antarctic Mode Water, Antarctic Intermediate Water (AAIW), Upper Circumpolar Deep Water (UCDW), and North Atlantic Deep Water (NADW). Core 90GGC sits within the core of AAIW as outlined by the low-salinity tongue emanating from the Southern Ocean. In the South Atlantic, low carbonate ion in the 1,200- to 1,800-m depth range reflects the influence of UCDW, while low values in the tropics reflect the influence of remineralization associated with upwelling (Gebbie, 2014). The inset map shows the location of the A17 section relative to the core sites (white circle).

early Holocene (Lund et al., 2015). However, in the early deglacial interval of the core (105 to 150 cm), there is evidence of displacement of planktonic foraminifera from the late deglacial portion of the stratigraphy despite no evidence of displaced benthics (Lund et al., 2015). Similar to some other Brazil Margin sites, it appears that burrowing from upsection, where the ratio of planktonic to benthic shells can be ~100 times higher, creates the unique situation where planktonic records are sensitive to burrowing, while the benthic time series are not. In the early deglacial section of 90GGC, we therefore created an additional age control point by aligning the positive benthic δ^{13}C excursion in 90GGC with that in KNR159-5-36GGC, a Brazil Margin core from 1,268-m depth with a better age model in the interval of interest (Table S1 in the supporting information). We also ran triplicate B/Ca analyses in the 100- to 150-cm interval of 90GGC to isolate any stratigraphically displaced samples.

2.2. B/Ca Calibration

B/Ca analyses were performed on the benthic foraminiferal species *Cibicidoides pachyderma*. Although previous B/Ca reconstructions from deeper sites have primarily relied on the epibenthic species *Cibicidoides*

wuellerstorfi, the overall abundance of *C. wuellerstorfi* at intermediate-depth sites is low because this represents the upper edge of its depth habitat (Van Morkhoven et al., 1986). We instead used *C. pachyderma* for the Brazil Margin site, which has a B/Ca sensitivity to $\Delta[CO_3^{2-}]$ similar to that of *C. wuellerstorfi* (Oppo et al., 2018). While calibrations for *C. wuellerstorfi* and *Cibicidoides mundulus* are based on globally distributed core top data (Yu & Elderfield, 2007), the current *C. pachyderma* calibration is regionally limited to data from the Demerara Rise off the northern coast of Brazil. As such, the number of data points in the calibration is considerably lower than for the other species ($n = 10$, $r^2 = 0.72$; Oppo et al., 2018). The 1σ calibration uncertainty in the B/Ca range of our samples is approximately ± 10 μmol/kg $[CO_3^{2-}]$. Despite the relatively limited number of data points, the core top calibration data set for *C. pachyderma* is the most appropriate for our study.

2.3. Foram Cleaning and Analysis

In this study, an average of three to four tests (>250-μm size fraction) were used for each analysis. Following the procedure outlined in Yu and Elderfield (2007), samples were crushed between two slides and homogenized with the aid of a high-powered reflected-light microscope. The chambers of *C. pachyderma* were finely ruptured in order to promote complete dissolution. Note that the following steps were conducted in a laminar flow hood with a B-free high-efficiency particulate air filter. Crushed samples were washed into 600-μl microcentrifuge tubes using Milli-Q water and ultrasonicated for 45 s to bring any clay present into suspension. Suspended clays were stirred and removed by squirting Milli-Q water into each tube and siphoning out the supernatant. This procedure was replicated twice, with additional rinses using methanol until sonication yielded a clear, particle-free fluid. A dual-haired picking brush was used to remove exceptionally discolored test fragments and foreign materials such as microscopic fibers and pyrite that remained after sonication. The samples then underwent oxidative cleaning to remove organic matter using a buffered H_2O_2 solution (100 μl 30% v/v H_2O_2 + 10 ml 0.1 M NaOH). Finally, samples were leached using a weak acid solution (0.001 M HNO_3) before dissolution in 500 μl of 2% HNO_3. Cleaned samples were analyzed for B/Ca using an Element-2 ICP-MS and ESI SC-2DX autosampler, where all samples were matrix matched to our 100-ppm [Ca] calibration standards. All cleaning and analysis was done at the UConn Avery Point Paleoclimate Laboratory.

2.4. Matrix Effects

Matrix effects stemming from small (5 to 20 ppm) Ca concentration mismatches between calibration standards and sample unknowns may bias B/Ca results. Yu et al. (2005) show that the accuracy of Cd/Ca and Zn/Ca ratios in standards decreases by ~10% and ~15%, respectively, when run at 180-ppm [Ca] versus 100-ppm [Ca]. However, trace elemental ratios Li/Ca, Mg/Ca, Al/Ca, Mn/Ca, and Sr/Ca yielded an accuracy of $\pm 2.5\%$ across a broad concentration range of 60- to 240-ppm [Ca]. To quantify matrix effects for B/Ca, we ran B/Ca standards with [Ca] ranging from 50 to 300 ppm using a 100-ppm calibration standard. We found that standards run in the 50- to 250-ppm range fell within $\pm 2.5\%$ of expected B/Ca values, while standards run at 300 ppm had B/Ca ratios 3% lower than their gravimetric values. These results suggest that matrix effects have a minimal influence on B/Ca analyses over a broad range of Ca concentrations.

To assess the potential influence of matrix effects on our unknowns, we subtracted the mean B/Ca at each depth from individual B/Ca values at the same depth and then plotted the residual B/Ca values versus [Ca] (Figure S1). The results indicate a ~0.2-μmol/mol B/Ca per ppm [Ca] relationship over the range of measured [Ca] values, suggesting a subtle but discernible matrix effect in our data. To assess whether this materially influenced the B/Ca time series for 90GGC, we plotted residual values versus depth in the core, where the residuals were calculated in two different ways. First, we estimated the residuals by subtracting the mean B/Ca at each depth from individual B/Ca values at the same depth (as in Figure S1). In the second case, we used a running mean calculated over a range of stratigraphic windows, including 10, 20, 25 and 30 cm (Figure S2). Regardless of the approach, we found no systematic relationship versus depth in the core. Thus, the observed downcore signal reflects reliable changes in B/Ca through time as opposed to any systematic bias associated with matrix effects.

2.5. Modern and Paleo-$[CO_3^{2-}]$

Modern carbonate ion concentrations for the Brazil Margin were estimated using the local and regional hydrographic parameters presented in Table 1. Potential temperature and salinity values at 1,100-m water

Table 1
Parameters for Estimating Modern [CO_3^{2-}] at the 90GGC Core Site

Water depth (m)	Potential temperature (°C)	S	PO_4^{3-} (μmol/kg)	SIO_3^{2-} (μmol/kg)	Avg. ALK (μmol/kg)	Avg. ΣCO_2 (μmol/kg)	[CO_3^{2-}] (μmol/kg)
1105	3.59	34.34	2.3	35	2,303 ± 21	2,189 ± 2	90 ± 10

depth were taken directly from CTD data collected during the KNR159-5 coring cruise. PO_4^{3-} and SIO_3^{2-} values were estimated using World Ocean Circulation Experiment (WOCE) Atlas Volume 3, section A10, which intersects the Brazil Margin at 28°S (http://whpatlas.ucsd.edu/whp_atlas/atlantic/a10/sections/sct_menu.htm). ALK and ΣCO_2 values were estimated using WOCE data from several stations (Table S2) located near our core site (http://www.ewoce.org/data/index.html#WHP_Bottle_Data). Given sloping isopycnal surfaces between the WOCE stations and the location of 90GGC, ALK and ΣCO_2 values were estimated using station data within ± 0.05 kg/m^3 of the potential density at the core site. We then estimated [CO_3^{2-}] using CO2SYS_v1.1 (Lewis, 2014). Carbonate ion saturation values were determined using the equation [CO_3^{2-}]$_{sat}$ = [CO_3^2]/$\Omega_{calcite}$, where $\Omega_{calcite}$ is the saturation state for calcite at a given water depth. Given [CO_3^{2-}]$_{sat}$ is primarily a function of depth, the assigned value is expected to have remained relatively unchanged from the LGM to the Holocene (Yu et al., 2008).

Downcore estimates of [CO_3^{2-}] were determined using the following empirical calibration: B/Ca = 1.134x + 102.35, where x is Δ[CO_3^{2-}] for *C. pachyderma* (Oppo et al., 2018). We then estimated [CO_3^{2-}] using the relationship [CO_3^{2-}] = Δ[CO_3^{2-}] + [CO_3^{2-}]$_{sat}$ (Table 1). Finally, our estimates of ΣCO_2 are based on the carbonate alkalinity relationship $\Sigma CO_2 \approx$ ALK $-$ [CO_3^{2-}]/0.6 (Yu et al., 2016).

2.6. Sources of Phosphate

WOCE observations of temperature, salinity, phosphate, dissolved oxygen, nitrate, δ^{13}C, and δ^{18}O (Gouretski & Koltermann, 2004) were inverted to determine water-mass pathways and the sources of phosphate in the subsurface ocean (Gebbie, 2014). The distribution of remineralized phosphate at the Brazil Margin is diagnosed as the difference between the observed phosphate and the distribution that would result if phosphate were a conservative tracer (i.e., the preformed value). This preformed value is calculated with the surface phosphate concentration and the water-mass fractions of the Brazil Margin as solved by the inversion. A second diagnostic is used to map the surface locations that are the source of the remineralized phosphate at the Brazil Margin. Assuming that the water-mass pathways represent a steady state circulation, we trace subsurface Brazil Margin waters back toward their surface sources and account for the locations where phosphate is added along the journey. We infer that the source of remineralized phosphate sources is biological productivity in the overlying surface ocean. Through this two-step tracking, we obtain a map of the surface sources of remineralized phosphate. Our estimates of remineralized phosphate are indirectly constrained by nitrate and oxygen through fixed stoichiometric ratios. Geometric constraints are also enforced, where remineralized phosphate can only increase as subsurface waters age (Gebbie & Huybers, 2010).

3. Results

The Brazil Margin [CO_3^{2-}] time series is characterized by three distinct intervals from the late LGM (18–20 kyr BP) to the early Holocene (8–10 kyr BP; Figure 2). During the late LGM, the mean [CO_3^{2-}] was 108 $\pm$ 1 μmol/kg, or ~20 μmol/kg higher than today (note that all uncertainties are presented as 1 standard error unless stated otherwise). From 18 to 16 kyr BP, [CO_3^{2-}] abruptly increased by ~22 μmol/kg, achieving a maximum value of 130 $\pm$ 2 μmol/kg during HS1. Over this same interval, benthic δ^{13}C increased by 0.4‰ $\pm$ 0.03‰, while benthic δ^{18}O decreased by 0.30‰ $\pm$ 0.05‰ (Curry & Oppo, 2005; Umling et al., 2019). The HS1 [CO_3^{2-}] maximum was followed by a gradual ~10-μmol/kg decline into the late Bølling-Allerød (~13 kyr BP). The beginning of the Younger Dryas (YD) marks a third inflection point in the [CO_3^{2-}] record, where values increased by ~5 μmol/kg followed by a slight decrease entering the early Holocene. Given the modern [CO_3^{2-}] value at the core site (90 $\pm$ 10 μmol/kg), we would expect that [CO_3^{2-}] decreased through the Holocene. However, the lack of *C. pachyderma* above 50-cm depth (8 kyr BP) precludes a comparison between core top and water-column [CO_3^{2-}] values.
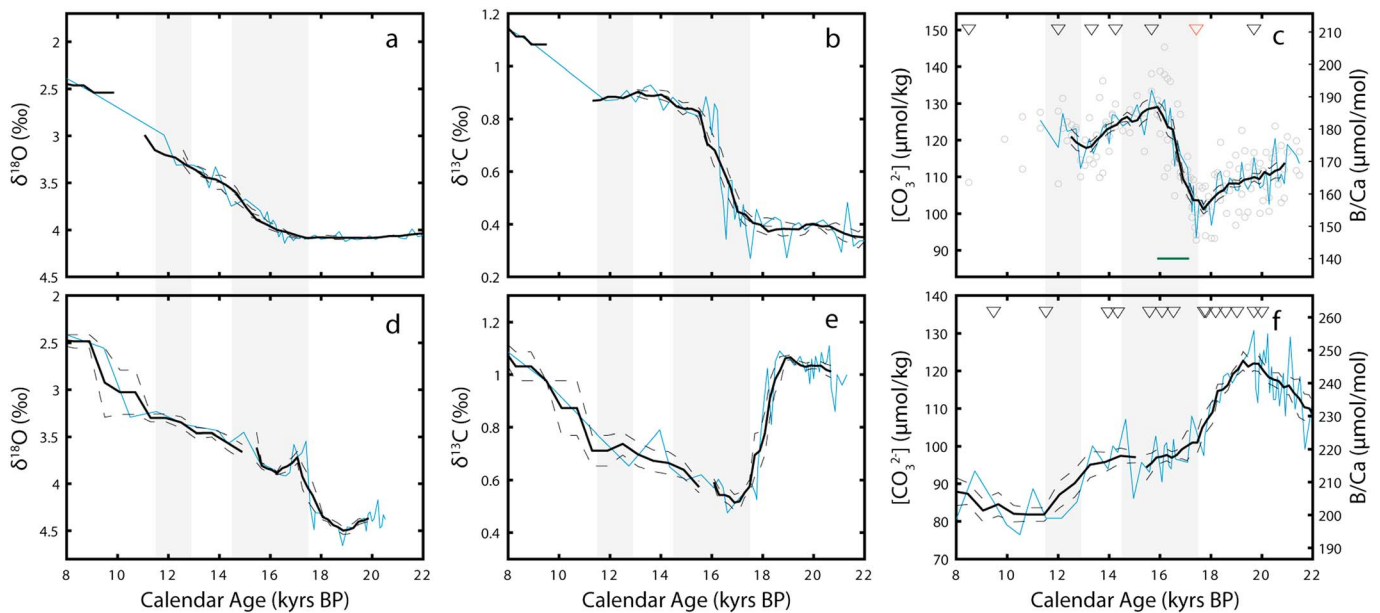
Figure 2. Benthic $\delta^{18}O$, $\delta^{13}C$, and B/Ca records for (top row) KNR159-5-90GGC and (bottom row) KNR159-5-78GGC. (a, d) Benthic $\delta^{18}O$, including the average value at each stratigraphic level (thin blue line), a 1.5-kyr running mean (thick black line), and ± 1 SE uncertainties (region between dashed lines). (b, e) Same as (a) and (d) but for $\delta^{13}C$. (c) *Cibicidoides pachyderma* B/Ca time series (right y-axis) with converted $[CO_3^{2-}]$ values (left y-axis), including individual values (open circles), average values at each stratigraphic level (thin blue line), 1-kyr running mean (thick black line), and ± 1 SE (region between dashed lines). (f) *Cibicidoides wuellerstorfi* B/Ca time series (right y-axis) with converted $[CO_3^{2-}]$ values (left y-axis) from Lacerra et al. (2017). Stable isotope data for 90GGC are from Umling et al. (2019), while radiocarbon data are from Lund et al. (2015). Radiocarbon age control points for 90GGC and 78GGC are shown as black triangles in (c) and (f), respectively. Core 90GGC also includes an additional age control point based on $\delta^{13}C$ comparison with core 36GGC (red triangle; see text for details). Carbonate ion concentrations for the *C. pachyderma* were estimated using the calibration from Oppo et al. (2018), while the $[CO_3^{2-}]$ values for *C. wuellerstorfi* are based on the Yu and Elderfield (2007) calibration. The thin green bar for 90GGC represents the depth interval with age reversals in planktonic foraminifera (Lund et al., 2015). While downcore burrowing likely impacted planktonic ^{14}C, there is no evidence of a similar phenomenon in the benthic $\delta^{18}O$, $\delta^{13}C$, and B/Ca records. Gray bars in each panel represent the Heinrich Stadial 1 (17.5–14.5 kyr BP) and Younger Dryas (12.9–11.5 kyr BP) intervals.

The 90GGC record displays the opposite $[CO_3^{2-}]$ signal of that recorded at two middepth (1,800–2,100 m) sites on the Brazil Margin. While all three records display the largest signal during HS1, results from 1,800 m imply that $[CO_3^{2-}]$ decreased by ~20 µmol/kg (Figure 2). A similar pattern occurred at 2,100-m water depth (Lacerra et al., 2017). The deeper sites also display a more gradual change, with $[CO_3^{2-}]$ values declining monotonically from ~18 to 15 kyr BP, while the 90GGC results appear to show a more abrupt deglacial shift from ~17 to 16 kyr BP. Consequently, the vertical gradient in $[CO_3^{2-}]$ between ~1 and 2 km changed markedly during the deglaciation, starting with little to no difference at 20 kyr BP and reaching an offset of 40 µmol/kg by 16 kyr BP (Figure 2).

4. Discussion

The abrupt increase in $[CO_3^{2-}]$ of ~20 µmol/kg suggests the intermediate-depth South Atlantic experienced a major shift in carbon cycling during HS1. Several factors could have contributed to the signal, including variations in alkalinity, CO_2 solubility, atmospheric pCO_2, biological remineralization, and outgassing from the Southern Ocean. Below we first address the ALK, solubility, and atmospheric CO_2 effects. After showing that these factors had little overall impact on $[CO_3^2]$, we then evaluate whether remineralization or outgassing was the more likely driver of the $[CO_3^{2-}]$ signal.

4.1. Alkalinity, Solubility, and Atmospheric pCO₂

Given that $[CO_3^{2-}]$ is a function of both alkalinity and ΣCO_2, increasing ALK could have caused the observed $[CO_3^{2-}]$ response. We believe this is unlikely, however, given that average changes in oceanic ALK would have a lagged response to any deglacial changes in carbonate preservation in the abyss. While local changes in the ALK associated with AAIW may have influenced the 90GGC record, model simulations of ALK anomalies 1,000 years after AMOC collapse show little change in the upper 1,500 m of the South
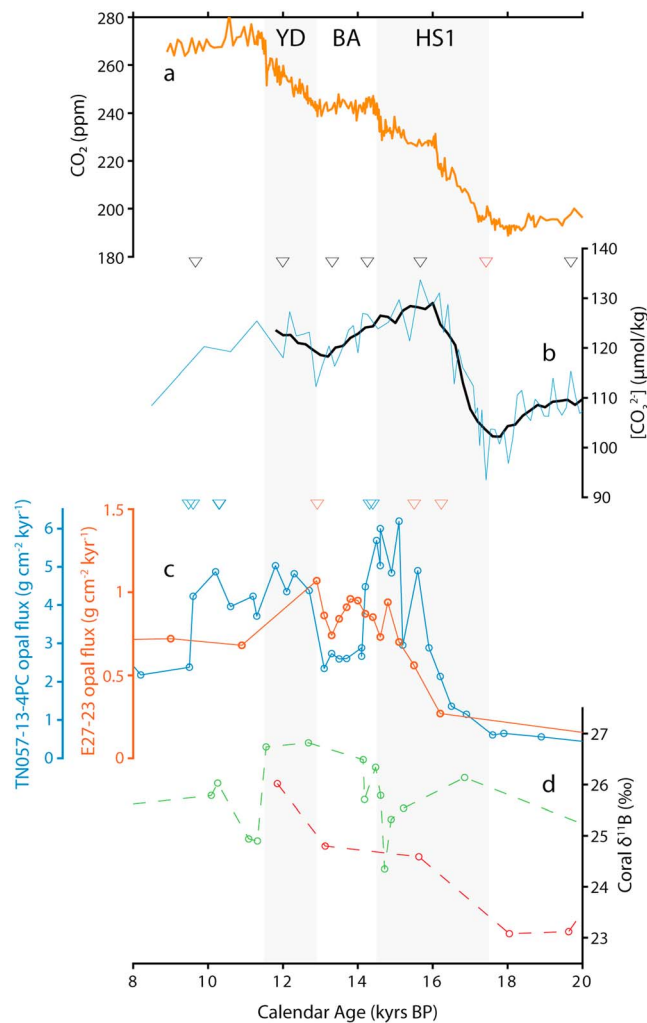
Figure 3. Carbon cycle proxy records spanning the last deglaciation. (a) Atmospheric CO_2 (Marcott et al., 2014) on the updated WD2014 age scale (Sigl et al., 2016). (b) Brazil Margin $[CO_3^{2-}]$ record from 1,100-m water depth (90GGC) where the thin black line represents the average value at each stratigraphic level and the thick black line represents a 1,000-year running mean. (c) Atlantic sector (blue; TN057-13PC; 53.2°S, 5.1°E) and Indian sector (orange; E27-23; 59°S, 155°E) Antarctic Zone opal flux records (g·cm[2]·kyr[1]; Anderson et al., 2009). (d) Drake Passage deep sea coral $\delta^{11}B$ results (Rae et al., 2018). The red dashed line is representative of sites closest to Antarctica, or the "deep" overturning cell in the Southern Ocean, while the green dashed line is representative of sites closer to South America, or the "shallow" overturning cell (see Rae et al., 2018, for details). Radiocarbon age control points for cores 90GGC, TN057-13PC, and E27-23 are marked as black, blue, and orange triangles respectively. Core 90GGC includes an additional age control point based on alignment with the $\delta^{13}C$ record in core 36GGC (red triangle; see text for details), and core E27-23 has an additional radiocarbon age control point at 20.2 kyr BP. YD = Younger Dryas; B-A = Bølling-Allerød; HS1 = Heinrich Stadial 1.

Atlantic (0–10 µmol/kg; Figure S3). The model used in Schmittner and Lund (2015) lacks an interactive sediment component, however, so we cannot rule out calcite dissolution as a source of ALK. Given that the core site is located well above the carbonate compensation depth, a local source of ALK is unlikely, so the signal would need to be driven by dissolution deeper in the water column. Yet the mid-depth $[CO_3^{2-}]$ signal is opposite that at intermediate depths, indicating that basin-scale alkalinity changes cannot account for the $[CO_3^{2-}]$ anomalies (Figure 2). If enhanced ΣCO_2 storage and $CaCO_3$ dissolution at mid-depths yielded a positive ALK signal at shallower sites, we would also expect such a signal to lag the mid-depth $[CO_3^{2-}]$ time series. Instead, $[CO_3^{2-}]$ at intermediate depth appears to lead the mid-depth carbonate ion record (Figure 2). Finally, the CO_3 record from Brazil Margin core 36GGC (1,270-m water depth) lacks a clear signal during HS1, implying there was little change in carbonate dissolution at intermediate depths (Figure S4). The available evidence therefore suggests that ALK played a minor role in the intermediate-depth $[CO_3^{2-}]$ response. Assuming that $\Sigma CO_2 \approx ALK - [CO_3^{2-}]/0.6$ (Yu et al., 2016), the $[CO_3^{2-}]$ data imply that ΣCO_2 decreased by approximately 37 µmol/kg during HS1.

The implied ΣCO_2 change may be related to weakening of the solubility pump. Several lines of evidence suggest that surface temperatures in Antarctica and the Southern Ocean warmed during the LGM-HS1 transition (Barker et al., 2009; Pedro et al., 2011; Shakun et al., 2012), which would decrease CO_2 solubility in surface waters and yield a negative ΣCO_2 signal at our core site. Of particular relevance is the surface temperature signal between the Polar Front and the Sub-Antarctic Front, where AAIW isopycnals outcrop to the surface Southern Ocean (Carter et al., 2008). To estimate surface temperatures in this zone, we use benthic $\delta^{18}O$ records from Brazil Margin cores 90GGC and 14GGC (440-m depth; Figure S6). While $\delta^{18}O$ in 90GGC should reflect sea surface temperatures (SSTs) in the source region for AAIW, the $\delta^{18}O$ from 14GGC will reflect SSTs in the source region for Sub-Antarctic Mode Water. Additionally, planktonic $\delta^{18}O$ results from the Brazil Margin based on the thermocline-dwelling *N. dutertrei* will be influenced by temperatures in the Subtropical Mode Water formation region where the Malvinas and Brazil Currents converge (Lund et al., 2019; Provost et al., 1999). Over the same time interval used to estimate the 90GGC $[CO_3^{2-}]$ signal, we estimate that benthic $\delta^{18}O$ decreased by 0.3‰ ± 0.05‰ in 90GGC and 0.5‰ ± 0.06‰ in 14GGC (Lund et al., 2015). By comparison, the change was somewhat smaller in the *N. dutertrei* record (0.20‰ ± 0.18 ‰; Hertzberg et al., 2016). If the $\delta^{18}O$ change was entirely due to temperature, the data imply that SSTs increased 1 to 2.5 °C. Assuming modern carbonate system parameters, the SST warming would yield an associated ΣCO_2 response of −18 ± 5 µmol/kg (Table S3). This is the maximum temperature effect because input of isotopically light melt water would act to lower surface water $\delta^{18}O$ in the Southern Ocean (and therefore benthic foraminiferal $\delta^{18}O$ at the Brazil Margin) Figure 3.

If rising temperatures were the only factor controlling preformed ΣCO_2 in the surface Southern Ocean, then a reduction in preformed ΣCO_2 could account for as much as 50% of the HS1 signal. However, atmospheric CO_2 concentrations also rose by ~30 ppm from the late LGM to mid-HS1 (Marcott et al., 2014), which would increase preformed ΣCO_2 in surface waters. Accounting for higher surface water pCO_2 and warming SSTs, the net change in preformed ΣCO_2 becomes +12 ± 5 µmol/kg. Rising atmospheric pCO_2 therefore more than

compensates for the solubility effect, implying that other factors must have caused the inferred ΣCO_2 decline at 90GGC during HS1.

While warming Southern Hemisphere SSTs likely influence Brazil Margin $\delta^{18}O$ records during HS1 (Pedro et al., 2011), the effect of subsurface warming due to AMOC collapse must also be considered. Liu et al. (2009) show that simulated weakening of the AMOC from an LGM state reduces convective heat exchange in the North Atlantic as well as northward heat transport, warming subsurface waters in the South Atlantic down to ~2,000-m water depth. At intermediate depths, simulated temperatures increased by 1.5 to 2 °C (Liu e al., 2009), somewhat smaller than the reconstructed HS1 signal for 90GGC based on the Mg/Li ratio of benthic foraminifera (2–3 °C; Umling et al., 2019). These results suggest that 75% to 100% of the $\delta^{18}O$ signal at the core site can be attributed to subsurface warming. If this was the case, there would have been little SST change in AAIW source regions during HS1. This scenario would require an alternative mechanism for reducing preformed ΣCO_2 or an even larger reduction in remineralization to explain the observed $[CO_3^{2-}]$ signal (see below).

4.2. Remineralization as a Driver of ΣCO_2 Decline

If collapse of the AMOC triggered the 90GGC $[CO_3^{2-}]$ response through modulation of the biological pump, then the magnitude of the observed signal should be similar to the modeled anomalies. The observed signal falls within the range of the simulated 20- to 30-µmol/kg increase in $[CO_3^{2-}]$ at intermediate depths (Figure 4). Note that there is a steep vertical gradient in the modeled anomalies in this depth range, with the signal doubling between 1,000- and 750-m water depth. Slight changes in the depth of this anomaly could therefore yield different estimates of the $[CO_3^{2-}]$ response. Furthermore, considering that the AMOC weakening simulations in Schmittner and Lund (2015) utilize preindustrial initial conditions, it is possible that future simulations using more realistic LGM initial conditions may yield different results. Nevertheless, the good agreement between modeled and observed $[CO_3^{2-}]$ anomalies suggests remineralization is a viable explanation of the $[CO_3^{2-}]$ trends in 90GGC. The agreement between modeled and observed $\delta^{13}C$ anomalies at this core site is also consistent with the biological pump mechanism (Figures 2 and S5; Hertzberg et al., 2016).

The positive shift in $[CO_3^{2-}]$ at intermediate depths occurs within ~1 kyr of negative shifts in $[CO_3^{2-}]$ at mid-depth Brazil Margin sites (Figure 2). Paired analysis of benthic $\delta^{13}C$ and $[CO_3^{2-}]$ suggests the mid-depth $\delta^{13}C$ anomalies are most likely due to accumulation of respired carbon associated with weakening of the AMOC (Lacerra et al., 2017). Mass balance calculations imply that remineralization can account for two thirds of the $\delta^{13}C$ signal at middepth, consistent with the proportion inferred through simulated collapse of the AMOC (Schmittner & Lund, 2015). We can use a similar approach to assess whether the deglacial $\delta^{13}C$ anomaly in 90GGC is consistent with remineralization. As in Lacerra et al. (2017), we use the following mass balance equations:

$$\left(\delta^{13}C_{Final}\right) \times \left(\Sigma CO_{2\ Final}\right) = \left(\delta^{13}C_{LGM}\right) \times \left(\Sigma CO_{2,LGM}\right) - \left(\delta^{13}C_{Removed}\right) \times \left(\Sigma CO_{2,Removed}\right) \tag{1}$$

$$\Sigma CO_{2,Final} = \Sigma CO_{2,LGM} - \Sigma CO_{2,Removed} \tag{2}$$

where $\delta^{13}C_{Final}$ represents $\delta^{13}C$ after the change in remineralization, $\delta^{13}C_{LGM}$ is the mean $\delta^{13}C$ prior to HS1 (18–20 kyr BP; 0.39‰ ± 0.03‰), $\Sigma CO_{2,\ Removed}$ is the estimated change in ΣCO_2 (37 µmol/kg), and $\delta^{13}C_{Removed}$ represents the mean value for marine organic carbon from 30°S to 60°S (−23‰ ± 2‰; Goericke & Fry, 1994). Finally, we assume $\Sigma CO_{2,\ LGM}$ was 2,200 µmol/kg, with a conservative error estimate of ±100 µmol/kg. Although estimates for $\Sigma CO_{2,\ LGM}$ currently do not exist, the assigned value has little influence on the final $\delta^{13}C$ estimate due to the small relative error (5%). Our mass balance calculation yields a $\delta^{13}C_{Final}$ of 0.79‰ ± 0.07‰, implying the change in $\delta^{13}C$ due to remineralization ($\delta^{13}C_{rem}$) was 0.4‰ ± 0.07‰. By comparison, the observed benthic $\delta^{13}C$ signal during the LGM-HS1 transition is 0.45‰ ± 0.04‰ (Figure 2). A reduction in remineralization equivalent to that implied by our B/Ca results could therefore explain 90‰ ± 20% of the $\delta^{13}C$ signal. The uncertainty in our estimate suggests that a positive shift in preformed $\delta^{13}C$ ($\delta^{13}C_{pre}$) could account for up to 30%. Because warming SSTs would have the opposite effect on $\delta^{13}C_{pre}$, any positive $\delta^{13}C_{pre}$ signal would require greater air-sea gas exchange.
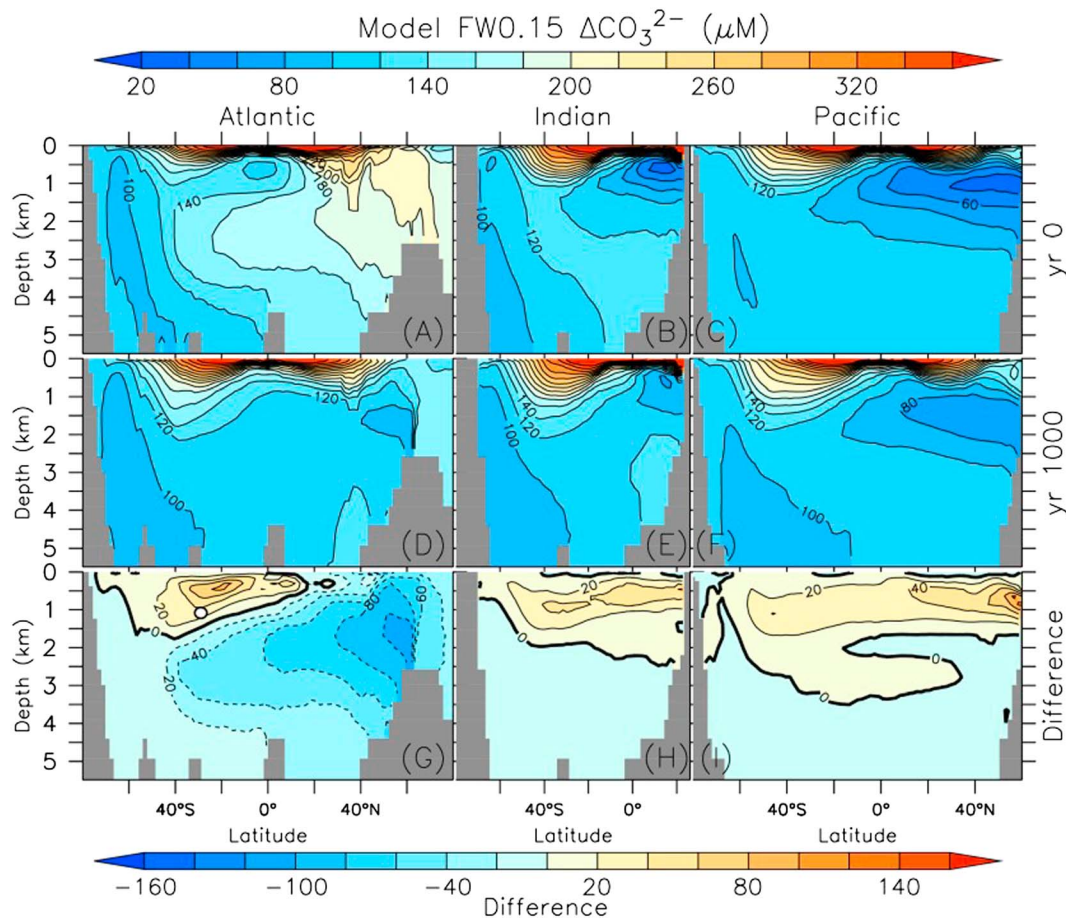
Figure 4. Simulated $[CO_3^{2-}]$ response due to Atlantic Meridional Overturning Circulation (AMOC) collapse (Schmittner & Lund, 2015). (a–c) Preindustrial $[CO_3^{2-}]$ for the Atlantic, Indian, and Pacific basins. (d–f) $[CO_3^{2-}]$ 1,000 years after AMOC shutdown. (g–i) The associated $[CO_3^{2-}]$ anomalies for each basin. The white circle in (g) marks the location of core 90GGC. Positive anomalies at intermediate depth reflect less input of remineralized carbon. The large negative anomalies in the middepth Atlantic are due to accumulation of light carbon (Schmittner & Lund, 2015).

The results of Umling et al. (2019) suggest that air-sea gas exchange signature of water masses bathing the site may account for the HS1 $\delta^{13}C$ signal. In their study, Cd/Ca (a proxy for ambient phosphate concentrations) in core 90GGC remains relatively constant throughout HS1 instead of decreasing as expected due to less remineralization (Schmittner & Lund, 2015) or deepening of the thermocline (Hain et al., 2014; Umling et al., 2019). Two or more mechanisms working in concert may have produced a net increase in $\delta^{13}C$ and no net change in Cd/Ca. One possibility is that the core site was influenced by a water mass with higher nutrients and a higher $\delta^{13}C$ air-sea ($\delta^{13}C_{as}$), which balanced the expected decline in nutrients (Umling et al., 2019). While such a mechanism would imply that remineralization played less of a role in driving the HS1 $\delta^{13}C$ signal, the $\delta^{13}C_{as}$ increase may have been compensated by a $\delta^{13}C$ decrease associated with a nutrient-rich water mass. If so, the observed benthic $\delta^{13}C$ response could still be attributed to reduced remineralization. It is also worth noting that the observed differences in Cd/PO$_4$ ratios between water masses (Middag et al., 2018) suggest that interpretation of Cd/Ca time series is not straightforward and may reflect the influence of different water mass mixtures at the core site. Regardless of the complexities associated with $\delta^{13}C$, the B/Ca on their own suggest that total ΣCO_2 increased during HS1, which we believe is most easily explained via remineralization.

4.3. Modern Context for the Remineralization Scenario

Remineralization plays a central role in setting $\delta^{13}C$ and phosphate levels at intermediate depths in the South Atlantic. Today, the concentration of remineralized phosphate at the 90GGC core site is
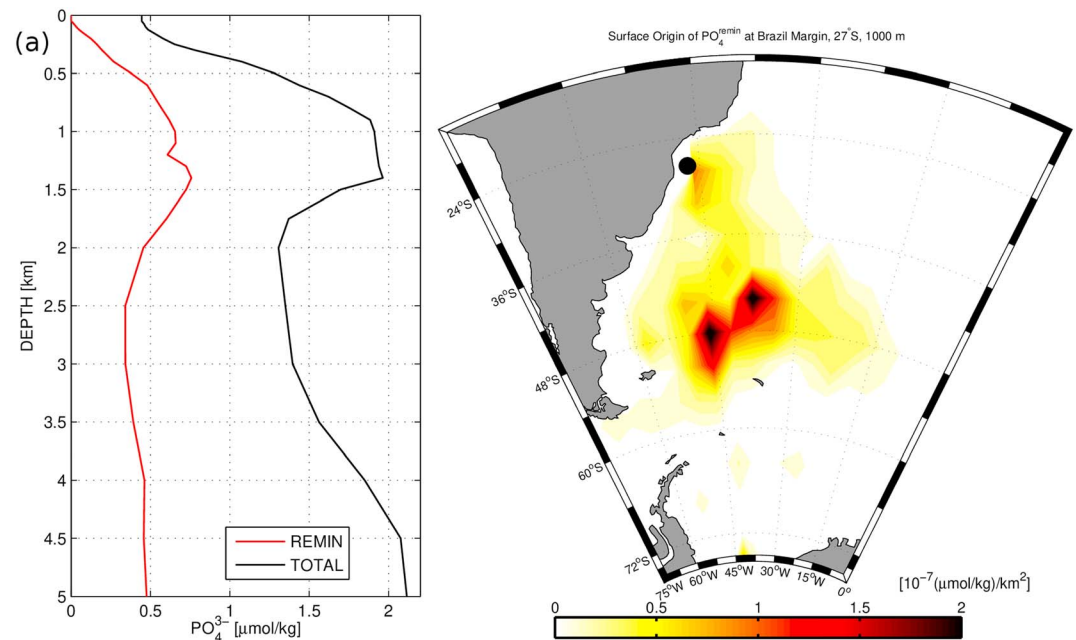
Figure 5. Phosphate in the South Atlantic. (a) Vertical profiles of total and remineralized phosphate at the Brazil Margin. At 1,000-m water depth, remineralized PO_4^{3-} accounts for 30–40% of the total phosphate. (b) Inferred source of remineralized PO_4^{3-} at 1,000 m on the Brazil Margin based on the tracer and flow field for the South Atlantic (see section 2 for details). Most of the remineralized PO_4^{3-} originates in the sub-Antarctic portion of the Southern Ocean. The black circle indicates the location of core 90GGC.

approximately 0.7 μmol/kg, or 35% of the total phosphate (Figure 5a). Assuming a C:P ratio for marine organic matter of 117:1 (Anderson & Sarmiento, 1994) and little change in local ALK, the 37-μmol/kg ΣCO_2 anomaly during HS1 is equivalent to a decrease in remineralized phosphate of approximately 0.3 μmol/kg, or ~40% of the modern remineralized component. Note that the fractional change may have been different during the LGM-HS1 transition due a higher baseline remineralized component during the LGM or shifts in Southern Ocean frontal positions that could influence the amount of remineralized carbon accumulated by AAIW on its path to the core site. Nevertheless, the modern values provide a useful point of comparison and suggest that the reconstructed change in remineralized phosphate during HS1 is not unreasonable.

Our water mass decomposition results show that the source of remineralized phosphate can be traced to the western South Atlantic and Southern Ocean, with the vast majority of the signal originating in the sub-Antarctic from 40°S to 60°S (Figure 5b). Maps of satellite-derived chl-a concentrations suggest this is one of the highest-productivity regions in the Southern Ocean (Deppeler & Davidson, 2017). Given the connection between remineralized phosphate at the Brazil Margin and biological productivity in the Southern Ocean, we suggest that the carbonate ion results in 90GGC reflect the influence of export production in the sub-Antarctic during the last deglaciation. In this sense, the core site may remotely monitor the Southern Ocean because (1) byproducts of respiration accumulate along the flow path of AAIW from the Southern Ocean to the core site and (2) there is relatively little local production of remineralized phosphate at the Brazil Margin due to its oligotrophic location (Figure 5b).

If the carbonate ion signal were entirely due to remineralization, our data would suggest that productivity in the western sub-Antarctic portion of the Southern Ocean decreased by ~40% relative to modern conditions. While this is a large signal, it is comparable to the simulated 10–40% decrease in export production associated with collapse of the AMOC (Schmittner, 2005). Note that this simulation is based on climatological winds, so it does not include the possibility of variable dust transport and iron fertilization in the sub-Antarctic (e.g., Martínez-García et al., 2014). Foram-bound iron flux, $\delta^{15}N$, and alkenone flux results from ODP Site 1090 both decrease during the LGM-HS1 transition, consistent with a weakening of the SAZ
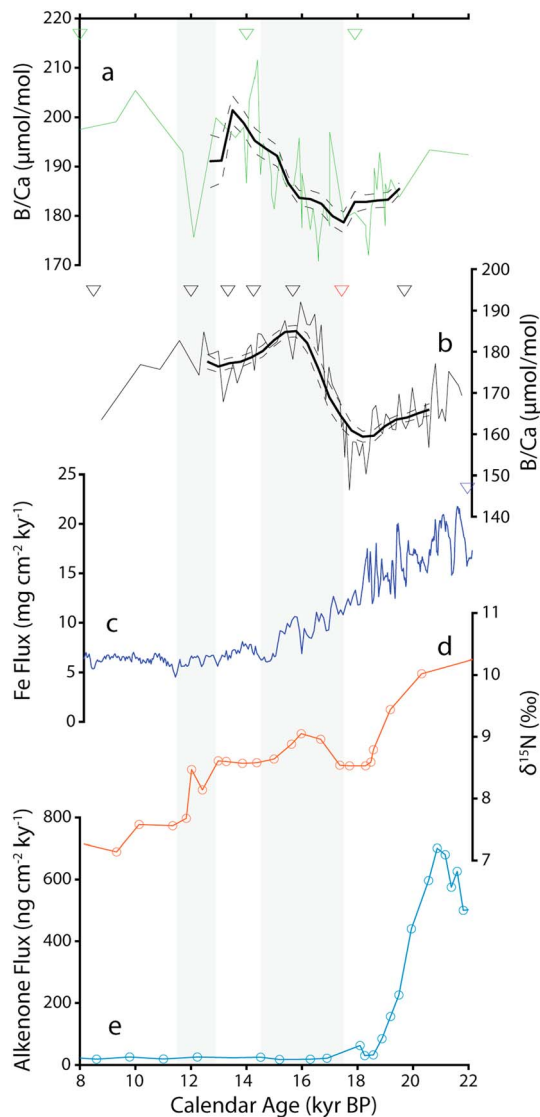
Figure 6. Southern Hemisphere carbon cycle and productivity proxies spanning the last deglaciation. (a) B/Ca results (μmol/mol) for core RR503-83 (37°S, 177°E; Allen et al., 2015), including average values at each stratigraphic level (thin green line), the 2,000-year running mean (solid black line), ±1 SE (area between dashed lines) and tephra layer age control points (green triangles). (b) B/Ca results for core 90GGC with the same plotting convention as in (a). Radiocarbon age control points for 90GGC are shown as black triangles, plus an additional age control point based on $\delta^{13}C$ comparison with core 36GGC (red triangle). (c) Fe flux (mg·cm^{-2}·kyr^{-1}) from ODP Site 1090 (42°S, 8°E, 3,702 m; Martínez-García et al., 2014) and (d) foraminifera-bound $\delta^{15}N$ (‰) from ODP Site 1090 (Martínez-García et al., 2014). (e) Alkenone flux (ng·cm^{-2}·kyr^{-1}) from core TN057-6, located immediately adjacent to ODP Site 1090 (Martínez-García et al., 2014). The gray shaded regions represent the Heinrich Stadial 1 interval (14.5–17.5 kyr BP) and Younger Dryas (12.9–11.5 kyr BP) interval, respectively. Age control (blue triangle) for (c–e) based on ice core chronology AICC2012 (Martínez-García et al., 2014).

biological pump (Martínez-Garcia et al., 2009; Martínez-García et al., 2014). However, the $\delta^{15}N$ and alkenone flux signals occur ~1,000 years prior to the 90GGC [CO_3^{2-}] signal (Figure 6), although this may be related to low sedimentation rates in ODP Site 1090 (2−3 cm/kyr) and age model uncertainty during HS1 (Martínez-García et al., 2014). The location of site 1090 (42°S, 8°E) also lies well outside of the implied source regions for remineralized phosphate for the Brazil Margin (Figure 5b). Furthermore, model reconstructions of glacial atmospheric dust flux to the Southern Ocean suggest values were highest in the western sub-Antarctic sector of the SAZ (Mahowald et al., 2006; Martínez-García et al., 2014), in close alignment with the remineralized phosphate map in Figure 5b. Additional compilations of dust flux, foram-bound $\delta^{15}N$, and alkenone flux results from the western sub-Antarctic portion of the Atlantic will be necessary to assess whether productivity was the driver of the [CO_3^{2-}] signal at the Brazil Margin.

If the Brazil Margin signal was predominately driven by variations in Southern Ocean productivity, then we would expect other intermediate-depth cores influenced by AAIW to show a similar change in [CO_3^{2-}]. One such reconstruction from core RR0503-83 at ~1,600-m water depth near New Zealand indicates that [CO_3^{2-}] increased by ~25 μmol/kg from 18 to 15 kyr BP (Allen et al., 2015). The magnitude is similar to that recorded at our core site, but the signal is delayed by approximately 1 kyr (Figure 6). The modern hydrography at RR0503-83 is primarily influenced by Upper Circumpolar Deep Water (UCDW), which sits just below AAIW at the core site location (Allen et al., 2015). Although Allen et al. (2015) interpreted the [CO_3^{2-}] record as evidence of carbon release from the deep ocean, their results could also reflect weakening of the biological pump. Indeed, the modeled [CO_3^{2-}] increase at 1,600-m near New Zealand due to remineralization is ~20 μmol/kg, which reflects downward mixing of the remineralization signal from intermediate depths (Figure 4). In this scenario, the lag between 90GGC and RR0503-83 may reflect the initial influence of reduced carbon flux to intermediate depths, followed by a delayed signal deeper in the water column due to mixing with UCDW.

4.4. Assessing the Deep Ventilation Hypothesis

Alternatively, the [CO_3^{2-}] signals in the SW Pacific and SW Atlantic may be related to enhanced outgassing of CO_2 in the Southern Ocean, as suggested by Allen et al. (2015). The air-sea flux of CO_2 is a function of the air-sea pCO_2 difference, the gas transfer velocity for CO_2, and the solubility of CO_2 in seawater (Takahashi et al., 2002). Given that atmospheric CO_2 increased by 35 ppmv during HS1, net flux out of the ocean would require an even larger increase in surface ocean pCO_2. As discussed in section 4.1, rising atmospheric CO_2 and reduced solubility due to warming in AAIW formation regions would have yielded little net change in surface ocean ΣCO_2 concentrations. Enhanced outgassing would therefore require higher ΣCO_2 values, most likely due to wind-driven upwelling of carbon-rich waters from the deep ocean (e.g., Anderson et al., 2009). Deep-sea coral $\delta^{11}B$ (a proxy for pH) data from the Drake Passage (Rae et al., 2018) and opal flux results from the Atlantic sector of the

Antarctic Zone (Anderson et al., 2009) suggest that abyssal carbon played an important role in the overall deglacial CO_2 rise. However, the largest changes in opal flux appear to occur after the initial 30-ppmv rise in atmospheric CO_2 (Figure 3). Furthermore, the resolution of the deep-sea coral results precludes a clear

assessment of the timing of pH variability during HS1. Transfer of CO_2 from the deep ocean to intermediate depths is most clearly observed in the converging $\delta^{11}B$ records at the end of HS1, at the approximate time of maximum opal flux (Figure 3).

Model results suggest that realistic changes in Southern Hemisphere westerly winds have only a modest influence on outgassing in the Southern Ocean (Menviel et al., 2018). An imposed 0.2-Sv decrease in freshwater flux to AABW formation regions, which doubles AABW production and drives upwelling of carbon-rich water from the abyss, combined with enhanced SW westerlies, yields a 20-ppmv increase in atmospheric CO_2 (Menviel et al., 2018). In this experiment, however, ΣCO_2 at intermediate depths in the South Atlantic increase by ~60 μmol/kg, opposite the signal implied by our $[CO_3^{2-}]$ results. Overall, the deglacial ΣCO_2 anomalies simulated by Menviel et al. (2018) are much larger than implied by published deep ocean $[CO_3^{2-}]$ reconstructions (Table S4). By comparison, weakening of the biological pump yields a better fit between simulated and estimated ΣCO_2 anomalies (Table S4 and Figure S7).

Can the expected change in $\delta^{13}C$ associated with deep upwelling be reconciled with the observed 0.4‰ increase of $\delta^{13}C$ in the Southwest Atlantic? One possible explanation is greater air-sea equilibration during HS1. Today, sub-Antarctic surface waters are characterized by $\delta^{13}C$ values up to 1‰ higher than expected from biological processes, apparently due to partial equilibration with the atmosphere at cold temperatures (Charles & Fairbanks, 1990; Oppo & Fairbanks, 1989). This "thermodynamic" $\delta^{13}C$ signal is carried northward by AAIW, with an imprint on $\delta^{13}C$ in the intermediate-depth South Atlantic of approximately 0.4‰ (Charles et al., 1993). Model results suggest that doubling of air-sea gas exchange yields 0.2–0.4‰ higher $\delta^{13}C_{DIC}$ in the surface Southern Ocean (Broecker & Maier-Reimer, 1992). Alternatively, the $\delta^{13}C$ signal may have been driven by AAIW mixing with a more nutrient-rich water mass with higher $\delta^{13}C_{as}$ (Umling et al., 2019). Changes to $\delta^{13}C_{as}$ could therefore feasibly produce the positive HS1 $\delta^{13}C$ at our core site. However, the proposed process would need to yield a signal large enough to overcome the combined effects of upwelling of light carbon in the Southern Ocean, exchange with a more ^{13}C-depleted atmosphere, and warmer equilibration temperatures. While we cannot rule out this scenario, we believe that the simpler explanation of the positive $\delta^{13}C$ anomaly during HS1 is reduced remineralization.

4.5. Longer-Term Variability

Following the LGM-HS1 transition, the 90GGC $[CO_3^{2-}]$ record varies in step with proxies of the AMOC while also displaying longer-term variability on glacial-interglacial time scales. If the biological pump weakened in response to an AMOC collapse early in HS1, then it should rebound during the Bølling-Allerød (B-A) when AMOC circulation was reinvigorated. In this scenario, we would expect a decrease in $[CO_3^{2-}]$ during the B-A (12.9–14.5 kyr BP) followed by an increase during the YD (11.5–12.9 kyr BP) when the AMOC collapsed again. Our $[CO_3^{2-}]$ record is broadly consistent with the expected pattern, showing that $[CO_3^{2-}]$ decreased ~10 μmol/kg during the B-A and rose ~5 μmol/kg during the YD (Figure 3). Note that there is a ~500-year (2σ) error for the 90GGC age model during the B-A (Lund et al., 2015), which complicates interpretation of this part of the record. Nonetheless, it appears the AMOC-modulated changes in the biological pump could account for the millennial-scale changes in $[CO_3^{2-}]$.

If $[CO_3^{2-}]$ responded primarily to AMOC-driven changes in the biological pump, then it should return to LGM levels upon strengthening of the AMOC after the YD. However, $[CO_3^{2-}]$ instead remained elevated throughout the remainder of the deglaciation and then declined slightly during the early Holocene (Figure 3). One important factor driving the observed trend was likely rising local ALK from mid-HS1 to ~12 kyr BP. During this interval, %$CaCO_3$ in core 36GGC (1,270-m water depth) increased by ~15%, indicating greater $CaCO_3$ preservation and higher ambient ALK concentrations, where higher ALK would prevent $[CO_3^{2-}]$ from decreasing back to LGM levels (Figure S4). Afer 12 kyr BP, %$CaCO_3$ remained persistently high into the Holocene and may explain higher intermediate-depth $[CO_3^{2-}]$ values observed at core 90GGC relative to during the LGM.

5. Conclusions

The mechanisms responsible for the rise in atmospheric CO_2 during the last deglaciation have been a primary focus of paleoclimatologists for over 30 years. In this study, we propose that the initial ~30-ppmv

rise in atmospheric CO_2 may be explained by a reduction in global average biological pump efficiency, a result of (1) reduced AMOC circulation, (2) less complete consumption of macronutrients in the SAZ in response to changes in iron fertilization, or a combination of the two. Here we explore past variability in upper ocean carbon cycling by reconstructing $[CO_3^{2-}]$ using an intermediate-depth core from the Southwest Atlantic. Our results show a pronounced increase in $[CO_3^{2-}]$ that was contemporaneous with the initial rise in atmospheric CO_2. Given that rising atmospheric CO_2 would compensate for reduced CO_2 solubility associated with warmer SSTs, we infer that the carbonate ion signal reflects reduced accumulation of remineralized carbon from the AAIW formation region to the core site.

Mass balance calculations suggest that the majority of the $\delta^{13}C$ signal during the LGM to HS1 transition can be explained by reduced input of remineralized carbon, though we cannot rule out changes in air-sea gas exchange in AAIW source regions as an alternative driver. Modern AAIW carries a large remineralization signal, accounting for ~40% of the total phosphate concentrations at our core site relative to modern values. We propose that reduced export production in the sub-Antarctic region of the Southern Ocean imparted a large positive $[CO_3^{2-}]$ signal on intermediate-depth waters that was recorded in core 90GGC. Given the oligotrophic conditions in subtropical gyres and generally abundant carbonate in underlying sediments, locations such as 90GGC may be used for remotely monitoring export production in the sub-Antarctic. Though records of nutrient utilization efficiency and export production from the Atlantic sector of the SAZ exhibit the expected deglacial pattern under the biological pump hypothesis (Martínez-García et al., 2014), they are offset from the 90GGC $[CO_3^{2-}]$ signal by ~1,000 years. Considering the age model uncertainties and sedimentation rates associated with these records and their location in the Atlantic sector of the SAZ, future research should include direct investigation of surface ocean productivity changes in the Atlantic sector of the sub-Antarctic using high-resolution cores to determine whether productivity in these regions declined early in the deglaciation. Furthermore, while $[CO_3^{2-}]$ data from 1.6-km water depth in the South Pacific (Allen et al., 2015) are generally consistent with our results, the greater influence of UCDW at this location complicates comparison with our $[CO_3^{2-}]$ record. Thus, high-resolution $[CO_3^{2-}]$ time series from intermediate depths are also necessary to corroborate our results from the Southwest Atlantic.

References

Allen, K. A., Sikes, E. L., Hönisch, B., Elmore, A. C., Guilderson, T. P., Rosenthal, Y., & Anderson, R. F. (2015). Southwest Pacific deep water carbonate chemistry linked to high southern latitude climate and atmospheric CO_2 during the last glacial termination. *Quaternary Science Reviews*, *122*, 180–191. https://doi.org/10.1016/j.quascirev.2015.05.007

Anderson, L. A., & Sarmiento, J. L. (1994). Redfield ratios of remineralization determined by nutrient data analysis. *Global Biogeochemical Cycles*, *8*(1), 65–80. https://doi.org/10.1029/93GB03318

Anderson, R. F., Ali, S., Bradtmiller, L. I., Nielsen, S. H. H., Fleisher, M. Q., Anderson, B. E., & Burckle, L. H. (2009). Wind-driven upwelling in the Southern Ocean and the deglacial rise in atmospheric CO2. *Science*, *323*(5920), 1443–1448. https://doi.org/10.1126/science.1167441

Barker, S., Diz, P., Vautravers, M. J., Pike, J., Knorr, G., Hall, I. R., & Broecker, W. S. (2009). Interhemispheric Atlantic seesaw response during the last deglaciation. *Nature*, *457*(7233), 1097–1102. https://doi.org/10.1038/nature07770

Bauska, T. K., Baggenstos, D., Brook, E. J., Mix, A. C., Marcott, S. A., Petrenko, V. V., et al. (2016). Carbon isotopes characterize rapid changes in atmospheric carbon dioxide during the last deglaciation. *Proceedings of the National Academy of Sciences of the United States of America*, *113*(13), 3465–3470. https://doi.org/10.1073/pnas.1513868113

Bauska, T. K., Brook, E. J., Marcott, S. A., Baggenstos, D., Shackleton, S., Severinghaus, J. P., & Petrenko, V. V. (2018). Controls on millennial-scale atmospheric CO_2 variability during the last glacial period. *Geophysical Research Letters*, *45*, 7731–7740. https://doi.org/10.1029/2018GL077881

Bostock, H. C., Opdyke, B. N., Gagan, M. K., & Fifield, L. K. (2004). Carbon isotope evidence for changes in Antarctic Intermediate Water circulation and ocean ventilation in the southwest Pacific during the last deglaciation. *Paleoceanography*, *19*, PA4013. https://doi.org/10.1029/2004PA001047

Broecker, W. S., & Maier-Reimer, E. (1992). The influence of air and sea exchange on the carbon isotope distribution in the sea. *Global Biogeochemical Cycles*, *6*(3), 315–320. https://doi.org/10.1029/92GB01672

Carter, L., McCave, I. N., & Williams, M. J. (2008). Circulation and water masses of the Southern Ocean: A review. *Developments in Earth and Environmental Sciences*, *8*, 85–114. https://doi.org/10.1016/S1571-9197(08)00004-9

Charles, C. D., & Fairbanks, R. G. (1990). Glacial to interglacial changes in the isotopic gradients of Southern Ocean surface water. In *Geological History of the Polar Oceans: Arctic Versus Antarctic*, (pp. 519–538). Dordrecht: Springer. https://doi.org/10.1007/978-94-009-2029-3_30

Charles, C. D., Wright, J. D., & Fairbanks, R. G. (1993). Thermodynamic influences on the marine carbon isotope record. *Paleoceanography and Paleoclimatology*, *8*(6), 691–697. https://doi.org/10.1029/93PA01803

Chikamoto, M. O., Matsumoto, K., & Ridgwell, A. (2008). Response of deep-sea $CaCO_3$ sedimentation to Atlantic Meridional Overturning Circulation shutdown. *Journal of Geophysical Research*, *113*, G03017. https://doi.org/10.1029/2007JG000669

Curry, W. B., & Oppo, D. W. (2005). Glacial water mass geometry and the distribution of δ13C of ΣCO2 in the western Atlantic Ocean. *Paleoceanography*, *20*, PA1017. https://doi.org/10.1029/2004PA001021

Deppeler, S. L., & Davidson, A. T. (2017). Southern Ocean phytoplankton in a changing climate. *Frontiers in Marine Science*, *4*(40), 1–28. https://doi.org/10.3389/fmars.2017.00040

Farneti, R., & Delworth, T. L. (2010). The role of mesoscale eddies in the remote oceanic response to altered Southern Hemisphere winds. *Journal of Physical Oceanography*, *40*(10), 2348–2354. https://doi.org/10.1175/2010JPO4480.1

Gebbie, G. (2014). How much did glacial North Atlantic water shoal? *Paleoceanography*, *29*, 190–209. https://doi.org/10.1002/2013PA002557

Gebbie, G., & Huybers, P. (2010). Total matrix intercomparison: a method for determining the geometry of water-mass pathways. *Journal of Physical Oceanography*, *40*(8), 1710–1728. https://doi.org/10.1175/2010JPO4272.1

Goericke, R., & Fry, B. (1994). Variations of marine plankton $\delta^{13}C$ with latitude, temperature, and dissolved CO_2 in the world ocean. *Global Biogeochemical Cycles*, *8*(1), 85–90. https://doi.org/10.1029/93GB03272

Gouretski, V., & Koltermann, K. (2004). WOCE global hydrographic climatology. 644 Tech. Rep. 35, Berichte des Bundesamtes für Seeschifffahrt und Hydrographie.

Hain, M. P., Sigman, D. M., & Haug, G. H. (2010). Carbon dioxide effects of Antarctic stratification, North Atlantic Intermediate Water formation, and subantarctic nutrient drawdown during the last ice age: Diagnosis and synthesis in a geochemical box model. *Global Biogeochemical Cycles*, *24*, GB4023. https://doi.org/10.1029/2010GB003790

Hain, M. P., Sigman, D. M., & Haug, G. H. (2014). Distinct roles of the Southern Ocean and North Atlantic in the deglacial atmospheric radiocarbon decline. *Earth and Planetary Science Letters*, *394*, 198–208.

Hertzberg, J. E., Lund, D. C., Schmittner, A., & Skrivanek, A. L. (2016). Evidence for a biological pump driver of atmospheric CO_2 rise during Heinrich Stadial 1. *Geophysical Research Letters*, *43*, 12–242.

Ito, T., & Follows, M. J. (2005). Preformed phosphate, soft tissue pump and atmospheric CO_2. *Journal of Marine Research*, *63*(4), 813–839. https://doi.org/10.1357/0022240054663231

Koutavas, A., & Lynch-Stieglitz, J. (2003). Glacial-interglacial dynamics of the eastern equatorial Pacific cold tongue-Intertropical Convergence Zone system reconstructed from oxygen isotope records. *Paleoceanography*, *18*(4), 1089. https://doi.org/10.1029/2003PA000894

Lacerra, M., Lund, D., Yu, J., & Schmittner, A. (2017). Carbon storage in the mid-depth Atlantic during millennial-scale climate events. *Paleoceanography*, *32*, 780–795. https://doi.org/10.1002/2016PA003081

Lewis, E. (2014). Interactive comment on "Comparison of seven packages that compute ocean carbonate chemistry" by JC Orr et al.

Liu, Z., Otto-Bliesner, B. L., He, F., Brady, E. C., Tomas, R., Clark, P. U., et al. (2009). Transient simulation of last deglaciation with a new mechanism for Bølling-Allerød warming. *Science*, *325*(5938), 310–314. https://doi.org/10.1126/science.1171041

Lourantou, A., Lavrič, J. V., Köhler, P., Barnola, J.-M., Paillard, D., Michel, E., et al. (2010). Constraint on the CO_2 rise by new atmospheric carbon isotopic measurements during the last deglaciation. *Global Biogeochemical Cycles*, *24*, GB2015. https://doi.org/10.1029/2009GB003545

Lund, D., Hertzberg, J., & Lacerra, M. (2019). Carbon isotope minima in the South Atlantic during the last deglaciation: Evaluating the influence of air-sea gas exchange. *Environmental Research Letters*, *14*(5), 055004. https://doi.org/10.1088/1748-9326/ab126f

Lund, D. C., Tessin, A. C., Hoffman, J. L., & Schmittner, A. (2015). Southwest Atlantic water mass evolution during the last deglaciation. *Paleoceanography*, *30*, 477–494. https://doi.org/10.1002/2014PA002657

Mahowald, N. M., Muhs, D. R., Levis, S., Rasch, P. J., Yoshioka, M., Zender, C. S., & Luo, C. (2006). Change in atmospheric mineral aerosols in response to climate: Last glacial period, preindustrial, modern, and doubled carbon dioxide climates. *Journal of Geophysical Research*, *111*, D10202. https://doi.org/10.1029/2005jd006653

Marcott, S. A., Bauska, T. K., Buizert, C., Steig, E. J., Rosen, J. L., Cuffey, K. M., et al. (2014). Centennial-scale changes in the global carbon cycle during the last deglaciation. *Nature*, *514*(7524), 616–619. https://doi.org/10.1038/nature13799

Martin, J. H. (1990). Glacial-interglacial CO_2 change: The iron hypothesis. *Paleoceanography*, *5*(1), 1–13. https://doi.org/10.1029/PA005i001p00001

Martin, J. H., Knauer, G. A., Karl, D. M., & Broenkow, W. W. (1987). VERTEX: Carbon cycling in the northeast Pacific. *Deep Sea Research Part A. Oceanographic Research Papers*, *34*(2), 267–285. https://doi.org/10.1016/0198-0149(87)90086-0

Martínez-Garcia, A., Rosell-Melé, A., Geibert, W., Gersonde, R., Masqué, P., Gaspari, V., & Barbante, C. (2009). Links between iron supply, marine productivity, sea surface temperature, and CO_2 over the last 1.1 Ma. *Paleoceanography*, *24*, PA1207. https://doi.org/10.1029/2008pa001657

Martínez-García, A., Sigman, D. M., Ren, H., Anderson, R. F., Straub, M., Hodell, D. A., et al. (2014). Iron fertilization of the Subantarctic Ocean during the last ice age. *Science*, *343*(6177), 1347–1350. https://doi.org/10.1126/science.1246848

McManus, J. F., Francois, R., Gherardi, J., Keigwin, L. D., & Brown-Leger, S. (2004). Collapse and rapid resumption of Atlantic meridional circulation linked to deglacial climate changes. *Nature*, *428*(6985), 834–837. https://doi.org/10.1038/nature02494

Menviel, L., Spence, P., Yu, J., Chamberlain, M. A., Matear, R. J., Meissner, K. J., & England, M. H. (2018). Southern Hemisphere westerlies as a driver of the early deglacial atmospheric CO_2 rise. *Nature Communications*, *9*(1), 2503. https://doi.org/10.1038/s41467-018-04876-4

Middag, R., van Heuven, S. M., Bruland, K. W., & de Baar, H. J. (2018). The relationship between cadmium and phosphate in the Atlantic Ocean unravelled. *Earth and Planetary Science Letters*, *492*, 79–88. https://doi.org/10.1016/j.epsl.2018.03.046

Mix, A. C., Pisias, N. G., Zahn, R., Rugh, W., Lopez, C., & Nelson, K. (1991). Carbon 13 in Pacific Deep and Intermediate Waters, 0-370 ka: Implications for ocean circulation and Pleistocene CO_2. *Paleoceanography and Paleoclimatology*, *6*(2), 205–226. https://doi.org/10.1029/90PA02303

Monnin, E., Indermühle, A., Dällenbach, A., Flückiger, J., Stauffer, B., Stocker, T. F., et al. (2001). Atmospheric CO_2 concentrations over the last glacial termination. *Science*, *291*(5501), 112–114. https://doi.org/10.1126/science.291.5501.112

Oppo, D. W., & Fairbanks, R. G. (1989). Carbon isotope composition of tropical surface water during the past 22,000 years. *Paleoceanography and Paleoclimatology*, *4*(4), 333–351. https://doi.org/10.1029/PA004i004p00333

Oppo, D. W., Gebbie, G., Huang, K. F., Curry, W. B., Marchitto, T. M., & Pietro, K. R. (2018). Data constraints on glacial Atlantic water mass geometry and properties. *Paleoceanography and Paleoclimatology*, *33*, 1013–1034. https://doi.org/10.1029/2018PA003408

Pahnke, K., & Zahn, R. (2005). Southern Hemisphere water mass conversion linked with North Atlantic climate variability. *Science*, *307*(5716), 1741–1746. https://doi.org/10.1126/science.1102163

Pedro, J. B., Van Ommen, T. D., Rasmussen, S. O., Morgan, V. I., Chappellaz, J., Moy, A. D., et al. (2011). The last deglaciation: Timing the bipolar seesaw. *Climate of the Past*, *7*(2), 671–683. https://doi.org/10.5194/cp-7-671-2011

Provost, C., Escoffier, C., Maamaatuaiahutapu, K., Kartavtseff, A., & Garçon, V. (1999). Subtropical mode waters in the South Atlantic Ocean. *Journal of Geophysical Research*, *104*(C9), 21,033–21,049. https://doi.org/10.1029/1999JC900049

Rae, J. W., Burke, A., Robinson, L. F., Adkins, J. F., Chen, T., Cole, C., et al. (2018). CO_2 storage and release in the deep Southern Ocean on millennial to centennial timescales. *Nature*, *562*(7728), 569–573. https://doi.org/10.1038/s41586-018-0614-0

Rae, J. W. B., Foster, G. L., Schmidt, D. N., & Elliott, T. (2011). Boron isotopes and B/Ca in benthic foraminifera: Proxies for the deep ocean carbonate system. *Earth and Planetary Science Letters*, *302*(3-4), 403–413. https://doi.org/10.1016/j.epsl.2010.12.034

Schlitzer, R. (2015). Ocean Data View. [Available at http://odv.awi.de.].

Schmittner, A., Brook, E. J., & Ahn, J. (2007). Impact of the ocean's overturning circulation on atmospheric CO$_2$. In *Ocean Circulation: Mechanisms and Impacts*, *AGU Geophysical Monograph Series*, (Vol. 173, pp. 209–246). Washington, D. C: AGU.

Schmittner, A., & Galbraith, E. D. (2008). Glacial greenhouse-gas fluctuations controlled by ocean circulation changes. *Nature*, *456*(7220), 373–376. https://doi.org/10.1038/nature07531

Schmittner, A., Gruber, N., Mix, A. C., Key, R. M., Tagliabue, A., & Westberry, T. K. (2013). Biology and air–sea gas exchange controls on the distribution of carbon isotope ratios (δ^{13}C) in the ocean. *Biogeosciences*, *10*(9), 5793–5816. https://doi.org/10.5194/bg-10-5793-2013

Schmittner, A., & Lund, D. C. (2015). Early deglacial Atlantic overturning decline and its role in atmospheric CO$_2$ rise inferred from carbon isotopes (δ^{13}C). *Climate of the Past*, *11*(2), 135–152. https://doi.org/10.5194/cp-11-135-2015

Schmittner, A. (2005). Decline of the marine ecosystem caused by a reduction in the Atlantic overturning circulation. *Nature*, *434*(7033), 628–633. https://doi.org/10.1038/nature03476

Shakun, J. D., Clark, P. U., He, F., Marcott, S. A., Mix, A. C., Liu, Z., et al. (2012). Global warming preceded by increasing carbon dioxide concentrations during the last deglaciation. *Nature*, *484*(7392), 49–54. https://doi.org/10.1038/nature10915

Siegel, D. A., Buesseler, K. O., Doney, S. C., Sailley, S. F., Behrenfeld, M. J., & Boyd, P. W. (2014). Global assessment of ocean carbon export by combining satellite observations and food-web models. *Global Biogeochemical Cycles*, *28*, 181–196. https://doi.org/10.1002/2013GB004743

Sigl, M., Fudge, T., Winstrup, M., Cole-Dai, J., Ferris, D., Mcconnell, J., et al. (2016). The WAIS Divide deep ice core WD2014 chronology—Part 2: Annual-layer counting (0–31 ka BP). *Climate of the Past*, *12*(3), 769–786. https://doi.org/10.5194/cp-12-769-2016

Sigman, D. M., Hain, M. P., & Haug, G. H. (2010). The polar ocean and glacial cycles in atmospheric CO$_2$ concentration. *Nature*, *466*(7302), 47–55. https://doi.org/10.1038/nature09149

Spero, H. J., & Lea, D. W. (2002). The cause of carbon isotope minimum events on glacial terminations. *Science*, *296*(5567), 522–525. https://doi.org/10.1126/science.1069401

Takahashi, T., Sutherland, S. C., Sweeney, C., Poisson, A., Metzl, N., Tilbrook, B., et al. (2002). Global sea–air CO$_2$ flux based on climatological surface ocean pCO$_2$, and seasonal biological and temperature effects. *Deep Sea Research Part II: Topical Studies in Oceanography*, *49*(9-10), 1601–1622. https://doi.org/10.1016/S0967-0645(02)00003-6

Toggweiler, J. R., Gnanadesikan, A., Carson, S., Murnane, R., & Sarmiento, J. L. (2003). Representation of the carbon cycle in box models and GCMs: 1. Solubility pump. *Global Biogeochemical Cycles*, *17*(1), 1026. https://doi.org/10.1029/2001gb001401

Toggweiler, J. R., Russell, J., & Carson, S. R. (2006). Midlatitude westerlies, atmospheric CO$_2$, and climate change during the ice ages. *Paleoceanography*, *21*, PA2005. https://doi.org/10.1029/2005PA001154

Umling, N. E., Oppo, D. W., Chen, P., Yu, J., Liu, Z., Yan, M., et al. (2019). Atlantic circulation and ice sheet influences on upper South Atlantic temperatures during the last deglaciation. *Paleoceanography and Paleoclimatology*, *34*, 990–1005. https://doi.org/10.1029/2019PA003558

Van Morkhoven, F. P. C., Berggren, W. A., & Edwards, A. S. (1986). *Cenozoic cosmopolitan deep-water benthic foraminifera*, (p. 50). Pau, France: Elf-Aquitaine.

Yu, J., Broecker, W. S., Elderfield, H., Jin, Z., McManus, J., & Zhang, F. (2010). Loss of carbon from the deep sea since the Last Glacial Maximum. *Science*, *330*(6007), 1084–1087. https://doi.org/10.1126/science.1193221

Yu, J., Day, J., Greaves, M., & Elderfield, H. (2005). Determination of multiple element/calcium ratios in foraminiferal calcite by quadrupole ICP-MS. *Geochemistry, Geophysics, Geosystems*, *6*, Q08P01. https://doi.org/10.1029/2005GC000964

Yu, J., Elderfield, H., & Piotrowski, A. M. (2008). Seawater carbonate ion-δ^{13}C systematics and application to glacial–interglacial North Atlantic ocean circulation. *Earth and Planetary Science Letters*, *271*(1-4), 209–220. https://doi.org/10.1016/j.epsl.2008.04.010

Yu, J., Menviel, L., Jin, Z. D., Thornalley, D. J. R., Barker, S., Marino, G., et al. (2016). Sequestration of carbon in the deep Atlantic during the last glaciation. *Nature Geoscience*, *9*(4), 319–324. https://doi.org/10.1038/NGEO2657

Yu, J. M., & Elderfield, H. (2007). Benthic foraminiferal B/Ca ratios reflect deep water carbonate saturation state. *Earth and Planetary Science Letters*, *258*(1-2), 73–86. https://doi.org/10.1016/j.epsl.2007.03.025